# Power optimization and economic evaluation of thermoelectric waste heat recovery system around a rotary cement kiln

M. Hosseini, S. Mojtaba; Rezaniakolaei, Alireza; Rosendahl, Lasse

*Published in:*
Journal of Cleaner Production

*DOI (link to publication from Publisher):*
10.1016/j.jclepro.2019.06.011



*Publication date:*
2019

*Document Version*
Accepted author manuscript, peer reviewed version

# Accepted Manuscript

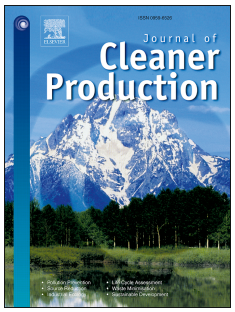


Power optimization and economic evaluation of thermoelectric waste heat recovery system around a rotary cement kiln

Mojtaba Mirhosseini, Alireza Rezania, Lasse Rosendahl

PII: S0959-6526(19)31955-9

DOI: https://doi.org/10.1016/j.jclepro.2019.06.011

Reference: JCLP 17180

To appear in: *Journal of Cleaner Production*

Received Date: 4 September 2018

Revised Date: 31 May 2019

Accepted Date: 1 June 2019

Please cite this article as: Mirhosseini M, Rezania A, Rosendahl L, Power optimization and economic evaluation of thermoelectric waste heat recovery system around a rotary cement kiln, *Journal of Cleaner Production* (2019), doi: https://doi.org/10.1016/j.jclepro.2019.06.011.

# Power Optimization and Economic Evaluation of Thermoelectric Waste Heat Recovery System around a Rotary Cement Kiln

**Mojtaba Mirhosseini [1,*], Alireza Rezania [2], Lasse Rosendahl [3]**

[1,*] First and corresponding author, Email: seh@et.aau.dk

[2] Second author, Email: alr@et.aau.dk

[3] Third author, Email: lar@et.aau.dk

Department of Energy Technology, Aalborg University, Pontoppidanstraede 111, 9220 Aalborg East, Denmark

# Power Optimization and Economic Evaluation of Thermoelectric Waste Heat Recovery System around a Rotary Cement Kiln

**Mojtaba Mirhosseini*, Alireza Rezania, Lasse Rosendahl**

Corresponding author: seh@et.aau.dk,
mojtaba27900@gmail.com

Department of Energy Technology, Aalborg University, Pontoppidanstraede 111, 9220 Aalborg East, Denmark

**Abstract**

Cement rotary kiln is the main device utilized for industrial cement production in large scale. The shell temperature can reach several hundred Celsius degrees. Therefore, a thermoelectric waste heat recovery system can be utilized based on its advantages. In this study, an arc shaped absorber is designed and temperature distribution along the absorber circumference is obtained numerically. The calculated temperature is considered as the hot side temperature of thermoelectric generators (TEGs) that recover thermal energy on the absorber. In situations where the heat is free, the metric for designing a thermoelectric system is to reach the maximum power output. In order to reach regional optimal power from parametric design, the absorber length is divided into several sections. For efficient design of the TEG in each section, effect of significant parameters such as leg length and fill factor of the TEG and thermal resistance of the heat sink are studied. Effect of variation of the temperature and velocity magnitudes of the air next to the heat sinks is considered on thermal resistance and performance of the pin-fin heat sinks along the absorber. β-phase zinc antimonide ($Zn_4Sb_3$) and magnesium tin silicide ($Mg_2SiSn$) are chosen as the p- and n-leg thermoelectric materials of the TEGs, respectively, because of their relatively high performance over the considered range of operating temperature. The results show that, staggered arrangement of the pin-fins is more effective for higher power generation and system performance compared to in-line arrangement of the fins. Moreover, by evaluation of the results, maximum matched power output in each section versus the fill factor and leg length can be determined in this study. The results show that, low fill factors between 0.05 and 0.2 can provide relatively a same maximum power as high fill factors. Furthermore, an economic evaluation is carried out to find optimal design of the TEG device for highest power generation and lowest investment cost. Various parameters of the cost function, such as cost of the bulk raw material ($C_B$), manufacturing cost associated with processing bulk material ($C_{M,B}$), areal manufacturing cost ($C_{M,A}$), heat exchanger cost ($C_{H\text{-}EX}$), balance of the system cost ($C_{BoS}$) and the installation cost ($C_I$) are taken into account in this study. The results show dominant parameter in the system cost is the heat sink.

*Keywords:* Cement Rotary Kiln; Waste Heat Recovery; Thermoelectric System; Theoretical Modelling; Design Optimization; Total Investment Cost.

## 1. Introduction

In cement rotary kilns, significant amount of the thermal energy is lost from the kiln shell (Liu et al., 2018; Karellas et al., 2013), while thermoelectric generators (TEGs) can be utilized for waste heat recovery and direct conversion of the heat into electricity.

Although the TEGs should not be installed directly on the kiln shell, due to increment in kiln weight needing more energy for rotation of the kiln, the distance between the TEG system and the rotary kiln should be preferably as small as possible. Moreover, a surface to surface contact between the TEGs and the kiln increases temperature on the kiln shell that can cause cracks on the kiln shell resulting from the hot spots. Therefore, design of a metallic frame as an absorber around the kiln with a specific gap from the kiln can support the heat recovery by the TEGs as well as to prevent the kiln from the increasing the weight and temperature.

For harvesting the waste heat from the cement rotary kiln, Hsu et al. (2013) designed and installed a TEG system to study energy conversion efficiency and economic impact of the system. The energy harvesting system, with 10 cm distance from the rotary kiln, generated a matched (or peak) power of 214 W for a long time. The generated power by the TEGs was used directly to light up indoor LED lamps and had a large contribution in saving the electrical energy. Luo et al. (2015) designed a TEG system to reduce heat loss from the cement rotary kilns. The system was designed as an array of TEGs configured longitudinally on a secondary shell coaxial with the cement kiln. In addition, a theoretical model was developed to estimate performance of the heat recovery system. The analytical results indicated that from a cement rotary kiln with diameter of 4.8 m and length of 72 m, 211 kW electrical power can be recovered.

Sztekler et al. (2017) investigated implementation of the TEG in a waste heat recovery system in a cement factory. Suitable position and design of the thermoelectric system applied to the cement plant were analysed by IPSEpro software. The length of their proposed system was 12 m with distance of 1 m underneath of the kiln in the form of arc shaped surface covering 1/6 of the kiln's circumference.

Mirhosseini et al. (2019b) designed an annular-shape heat recovery system around cement kiln in Aalborg Portland cement plant, Denmark. The average temperature on the absorber, as the hot side temperature of the TEG, was achieved and critical design parameters of the TEG such as leg length and fill factor were considered for system optimization. Their results show that zinc antimonide based TEG generated more power than the heat recovery system with bismuth telluride based TEG. One issue with the annular design of the absorber for heat recovery along the rotary kiln is that, the absorber acts as insulation and increases the surface temperature of the kiln, which reduces safety of the cement kiln. Therefore, in previous work, an arc shaped absorber was designed to investigate heat transfer features and fluid flow pattern around the kiln (Mirhosseini et al. 2018b). Although

various types of TEG-based heat recovery systems were considered by the above studies, there is lack of a comprehensive numerical study combining theoretical modelling and optimization of the TEG systems, including the heat sink geometry, coupled with the real operating and weather conditions around the kiln.

In this study, the heat transferred from the kiln to the absorber through the radiation and airflow pattern around the kiln is achieved. This study aims to design an optimal TEG system to maximize the power generation by dividing the arc shaped absorber into ten sections, where for each section, optimal design parameters of the TEG and heat sink are calculated individually. Furthermore, the economic assessment of the heat recovery sections is carried out in order to select the most desired design for highest power generation and lowest investment cost.

## 2. Numerical simulation and boundary conditions

Length of the Aalborg Portland rotary cement kiln is 163 m with outer diameter of 3.6 m for the primary length of 103 m. The diameter is 3.9 m for the rest of the kiln. The temperature distribution along the kiln in this study was measured and given by Aalborg Portland cement factory. According to the distribution along the kiln, the place with temperature of 500 °C is chosen for waste heat recovery. By using the temperature distribution, total heat loss from the cement kiln can be calculated. Since there is no experimental data measuring the heat loss from the kiln, the validation process in this study is carried out by comparing the analytical and numerical results.

In order to verify the heat transfer assessment, the wind velocity and radiative emissivity factor of the kiln external surface are taken 5.86 m/s and 1.0, respectively. The kiln external surface is supposed to be covered by a refractory paint with radiative emissivity factor close to the black body. Furthermore, the free stream air temperature and the rotational speed of the kiln are 278.15 K (5 $^{o}$C) and 5 rpm (clockwise), respectively. For better understanding of the heat transfer mechanism and physics of the flow around the kiln, both unsteady- and steady-state numerical solutions are compared to the analytical solution. More details about the numerical solution can be found in the previous work by Mirhosseini et al. (2018b and 2019b). Table 1 shows different kinds of heat losses from the kiln when the kiln surface temperature is taken 500 $^{o}$C.

Table 1: Validation of the numerical results in current study with analytical results for heat loss assessment from

the unit length of the cement kiln (without the absorber)

| | | Radiation [kW] | Free convection [kW] | Forced convection [kW] | Rotational convection [kW] | Total Convection [kW] | Total heat loss [kW] |
|---|---|---|---|---|---|---|---|
| Analytical solution | | 225.2961 | 39.3159 | 54.6566 | 26.6152 | 120.5877 | 345.8838 |
| Numerical solution | Unsteady model | 225.2678 | | -------- | | 69.5287 | 294.7966 |
| | Steady model | 225.2678 | | -------- | | 61.0038 | 286.2716 |

Table 1 shows that, the radiative heat loss is predicted accurate, whereas there is a difference between the analytical and numerical results for convective heat transfers. The heat transfer mechanism and physics of flow around the kiln are naturally complicated. The vortex shedding phenomenon, that affects the local properties around the kiln, causes a time dependent and periodic behaviour. Hence the unsteady simulation is able to estimate a better solution rather than the steady state. Moreover, the difference between the analytical and unsteady state solution is less than the difference between analytical and steady state solution. Accordingly, unsteady simulation is chosen for numerical part of the present study.

The main geometrical parameters of the absorber considered in this study are: $\alpha$, arc angle of the absorber, $\beta$, angle between the line passing through the midpoint of the absorber circumference and horizontal axis and $R$, inner radius of the absorber. The geometrical characteristics of $\alpha$=150°, $\beta$=30°, $R$=2.5m are selected as the optimized geometry of the absorber. The wind velocity, kiln rotational speed, and kiln external surface temperature are fixed at 4 m/s, 5 rpm (clockwise), and 773.15 K, respectively.

In order to enhance overall conversion efficiency in the present study, circumferential length of the absorber is divided into ten sections, so that in each section, the average temperature on the outer surface of that absorber section is considered as the hot side temperature of the TEG. Effect of significant parameters such as thermoelectric leg length, fill factor and thermal resistance of the heat sink are evaluated. Since the temperature and velocity of air flow corresponded to location of each heat sink are different, performance of the pin-fin heat sinks is studied individually in the coupled calculations in order to reach the maximum overall power generation. The $Zn_4Sb_3$ and $Mg_2SiSn$ are chosen as p- and n-types thermoelectric materials, respectively, because of high performance of these materials over the operating temperature range in this study. In Fig. 1, the temperature distribution along the absorber circumference is shown. The sectional average temperatures representing sectional hot side of the TEGs are also shown in this figure.

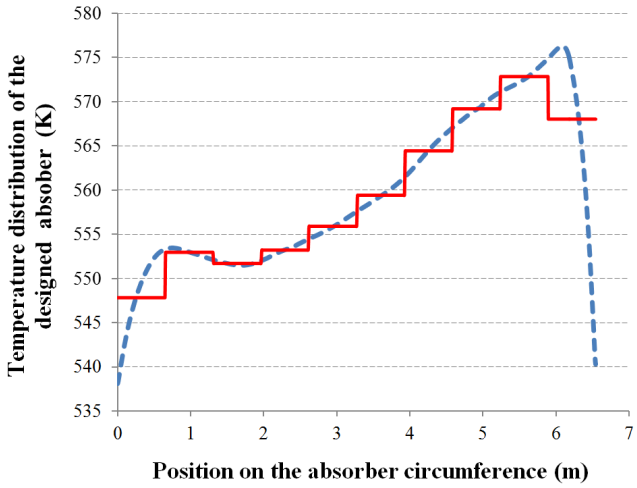


Fig. 1: Temperature distribution along the absorber circumference and sectional averaged temperatures

As mentioned, comprehensive numerical simulations are carried out to explore heat transfer features between the kiln and absorber and the temperature distribution along the absorber circumference. The average temperature and velocity of the air around outer surface of each section of the absorber, obtained by ANSYS software, 17.2, are presented in Table 2. The data is taken in 5 cm radial distance from the absorber outer surface, where represents the approximate location of the heat sinks. Figures 2a and 2b depict respectively a picture of Aalborg Portland cement factory and a schematic view of the thermal absorber. In Fig. 2c, the thermoelectric system is shown so that the radius of the absorber and the kiln are 2.5 and 1.8 m, respectively. The total length of the absorber circumference is 6542 mm. Therefore, the length of each section is about 654 mm. The same size is considered for the width of each section.

It should be noted that the data in Table 2 is for the two dimensional (2D) absorber without considering the pin fins. If the effect of the pin fins on the temperature and velocity distributions along the outer surface of the absorber is needed to be found, due to the big size of the system, simulation in three dimensions (3D), and presence of the pin-fin heat sinks on whole circumferential length of the absorber, run time is drastically increased.

Moreover, the pin fin heat sinks have lower resistance against the fluid flow in comparison with rectangular fins and other types. Accordingly, it seems the studied pin fin heat sinks do not have serious effect on flow and temperature distribution in this engineering case. On the other hand, it is conventional in a practical case to simplify and ignore some effects. In order for future works, the pin fins effect on the velocity and temperature distributions can be investigated by researchers.

A schematic view of different parts of the TEG unit for each section is shown in Fig. 3a. Fig. 3b shows a schematic view of the heat sink with considered geometrical parameters. In this design, the pin-fin heat exchangers are utilized on the cold side of the TEGs with two fin arrangements, i.e. in-line and staggered (Fig. 3c).

Table 2: Average temperature and velocity of the air around outer surface of each absorber section

| Section number | 1 | 2 | 3 | 4 | 5 | 6 | 7 | 8 | 9 | 10 |
|---|---|---|---|---|---|---|---|---|---|---|
| Temperature (K) | 323.465 | 314.47 | 313.559 | 312.976 | 313.668 | 315.445 | 317.637 | 329.142 | 326.299 | 335.233 |
| Velocity (m/s) | 0.83629 | 1.1193 | 2.04648 | 3.00673 | 3.1722 | 2.83165 | 2.48594 | 1.71793 | 1.07321 | 0.473289 |

(a)

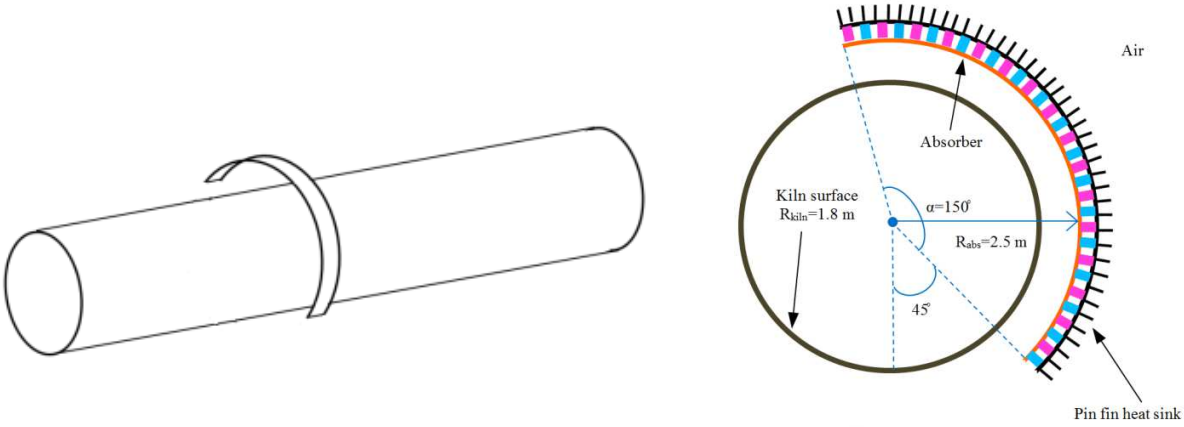


(b) (c)

Fig. 2: (a) Aalborg Portland cement kiln; (b) schematic view of the thermal absorber around the cement kiln where the kiln temperature is at 500 °C;

(c) TEG system designed on outer surface of the absorber

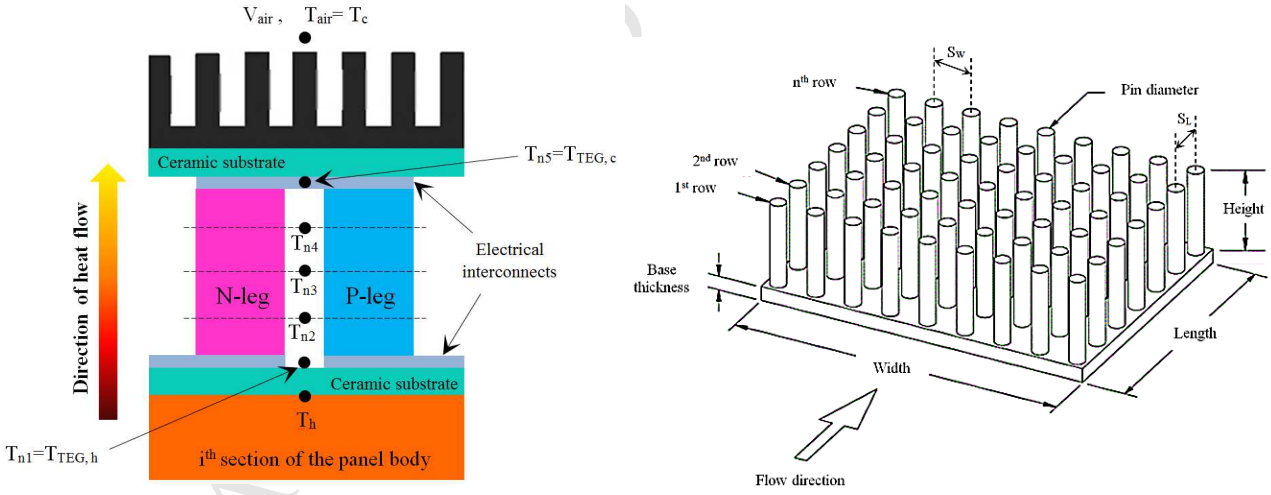


(a) (b)

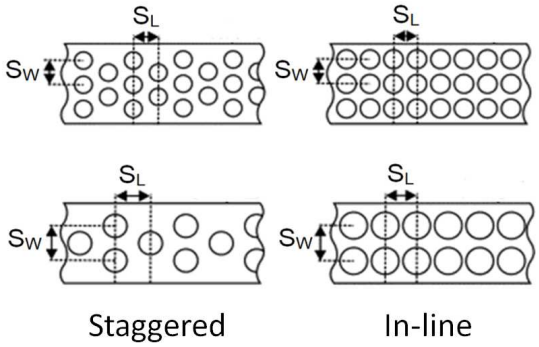


(c)

Fig. 3: (a) Components of the TEG device, (b) Pin-fin heat sink with considered geometrical parameters, (c) In-line and staggered pin-fin arrangements

## 3. Modelling of pin-fin heat sink

Several studies have investigated the effect of heat exchangers on performance of the TEG systems (Fernández-Yañez et al. 2018a, 2018b, 2018c; Rezania and Rosendahl, 2011, 2012a, 2012b). To calculate the thermal resistance of the die casting pin-fin heat sinks, analytical correlations for both in-line and staggered arrangements suggested in literature (Ndao et al. 2009) are used in this study. The thermal conductivity of the pure aluminium heat sink, $k_s$, is taken 237 W/mK (Touloukian et al. 1970). The air properties are calculated based on the air film temperature (Incropera et al. 2007) corresponding to each section. The temperature dependent properties of the air such as density ($\rho_f$), specific heat capacity ($C_{p,f}$), dynamic viscosity ($\mu_f$), thermal conductivity ($k_f$) and Prandtl number ($Pr_f$) are mentioned in Table 3, where the subscript index "*f*" expresses the properties at film temperature. The main correlation and related parameters are expressed as follow:

Table 3: Curve fitted properties of air

| | |
|---|---|
| Density (kg/m$^3$) | $363.42\,T^{-1.007}$ |
| Specific heat capacity (J/kgK) | $(2\times10^{-14})\,T^6-(6\times10^{-11})T^5+(7\times10^{-8})T^4-(4\times10^{-5})T^3+(1.3\times10^{-2})T^2-(2.1937)\,T+(1155.1)$ |
| Dynamic viscosity (Ns/m$^2$) | $[(-2\times10^{-4})T^2+(6.382\times10^{-1})T+(13.257)]\times10^{-7}$ |
| Thermal conductivity (W/mK) | $[(-3\times10^{-5})T^2+(9.8\times10^{-2})T-(1.668\times10^{-1})]\times10^{-3}$ |
| Prandtl number (-) | $(-4\times10^{-10})T^3+(10^{-6})T^2-(7\times10^{-4})T+(8.483\times10^{-1})$ |

$$\alpha=\frac{H}{d} \quad (1)$$

$$\beta=\frac{S_W}{d} \quad (2)$$

$$\lambda = \frac{S_L}{d} \tag{3}$$

$$D_h = \frac{4d(\beta-1)\lambda}{\pi} \tag{4}$$

$$Re_d = \frac{\rho_f V d}{\mu_f} \tag{5}$$

$$Nu_d = C_1 {Re_d}^{1/2} Pr^{1/3} \tag{6}$$

$$Re_L = \frac{\rho_f V L}{\mu_f} \tag{7}$$

$$Nu_L = C_1 {Re_L}^{1/2} Pr^{1/3} \tag{8}$$

$$Re_{D_h} = \frac{\rho_f V D_h}{\mu_f} \tag{9}$$

$$h_d = \frac{Nu_d k_f}{d} \tag{10}$$

$$m = \sqrt{\frac{4h_d}{k_s d}} \tag{11}$$

$$\eta_{fin} = \frac{\tanh(mH)}{mH} \tag{12}$$

$$R_{t-heat\ sink} = \frac{\left(\frac{1}{Nu_d k_f}\frac{1}{\pi\eta_{fin}}\frac{\beta\lambda d}{\alpha}\frac{1}{LW}\right)\left(\frac{1}{Nu_L k_f}\frac{L}{1-[\pi/(4\beta\lambda)]}\frac{1}{LW}\right)}{\left(\frac{1}{Nu_d k_f}\frac{1}{\pi\eta_{fin}}\frac{\beta\lambda d}{\alpha}\frac{1}{LW}\right)+\left(\frac{1}{Nu_L k_f}\frac{L}{1-[\pi/(4\beta\lambda)]}\frac{1}{LW}\right)} + \left(\frac{L}{C_{p,f}\mu_f}\frac{4}{Re_{D_h}}\frac{(\beta-1)\lambda}{\pi\alpha}\frac{1}{LW}\right) + \left(\frac{t}{k_s}\frac{1}{LW}\right) \tag{13}$$

where various geometric parameters are expressed as $H$, the pin height, $t$, the base thickness, $L$, the heat exchanger length, $W$, the heat exchanger width, $S_L$, distance between two adjacent pin-fins along the heat exchanger length, $S_W$, distance between two adjacent pin-fins along the heat exchanger width and $d$, pin diameter. For a straight pin-fin with uniform cross section and an adiabatic tip, the thermal efficiency is defined by Eq. 12. More details can be found in the results reported by Ndao et al. (2009). Parameter $C_1$ in Eq. 6 and 8 for in-line and staggered pin-fin arrangements, respectively, is obtained as follows:

$$C_{1-inline} = \frac{(0.2+e^{-0.55\beta})\beta^{0.785}\lambda^{0.212}}{(\beta-1)^{0.5}} \tag{14}$$

$$C_{1-staggered} = \frac{0.61\beta^{0.591}\lambda^{0.053}}{(\beta-1)^{0.5}(1-2e^{-1.09\beta})} \tag{15}$$

Finned heat exchangers increase the heat transfer area and, consequently, enhance heat transfer to the ambient. Three types of heat sinks are applied in this study (see Table 4). For each type of them, the thermal resistance of the heat sink in each section depends on boundary conditions.

Table 4: Different pin-fin heat sinks applied in this study

| | Heat sink I (in-line) | Heat sink II (in-line) | Heat sink III (staggered) |
|---|---|---|---|
| Fin height (m) | 0.05 | 0.01 | 0.05 |
| Base thickness (mm) | 2 | 2 | 2 |
| Heat sink length (m) | 0.65 | 0.65 | 0.65 |
| Heat sink width (m) | 0.65 | 0.65 | 0.65 |
| $S_L$ (mm) | 21.81 | 65.42 | 21.81 |
| $S_W$ (mm) | 21.81 | 65.42 | 21.81 |
| Pin diameter (mm) | 2 | 2 | 2 |

## 4. Design of thermoelectric waste heat recovery system

To design optimal thermoelectric unit for each section, one-dimensional (1D) thermal-electrical model is developed. The length of each thermoelectric leg is divided into four computational elements; hence, there are five nodes along each TEG leg. The effect of the Joule and Peltier heating is taken into account in the model. For $i^{th}$ element, half of the Joule heating ($Q_{Joule,ei}$) reaches the cold node and the other half is transferred to the hot node of the computational element. The heat transfer to $i^{th}$ node by the Peltier effect is expressed by $Q_{Peltier,ni}$. Effect of the Thomson heat is neglected in this research since it has small impact on the system performance in the considered range of the operating temperature (Goudarzi et al., 2014). The heat from each higher temperature node is conducted to its adjacent node with lower temperature. Therefore, with assuming zero side surface heat loss from the legs, a part of this heat is converted to electrical power by the element and rest of the heat transfers to the next node. Accordingly, Eqs. (16-46) can be written for the considered computational nodes. The thermal resistance at the hot side is expressed by $R_{t,h}$, and is used for calculation of the conductive heat transfer through the ceramic layer. Moreover, $R_{t,c}$, is the thermal resistance at the cold side consisting of the thermal resistance of the ceramic layer and the pin-fin heat sink. The energy balance in the nodes is shown in Eqs. 16, 22, 29, 36, and 43. More details about contribution of each term in the equations can be found in (Dunham et al. 2015; Hsiao et al. 2010).

**For the first node:**

$$\dot{Q}_h - \dot{Q}_{TE,e1} - \dot{Q}_{filler,e1} - \dot{Q}_{Peltier,n1} + \frac{\dot{Q}_{Joule,e1}}{2} = 0 \quad (16)$$

$$\dot{Q}_h = \frac{T_h - T_{n1}}{R_{t,h}} \quad (17)$$

$$\dot{Q}_{TE,e1} = \frac{T_{n1} - T_{n2}}{R_{t,TE,e1}} \quad (18)$$

$$\dot{Q}_{filler,e1} = \frac{T_{n1} - T_{n2}}{R_{t,filler,e1}} \quad (19)$$

$$\dot{Q}_{Peltier,n1} = n\, S_{e1}\, T_{n1}\, I \quad (20)$$

$$\dot{Q}_{Joule,e1} = I^2\, R_{e,TE,e1} \quad (21)$$

**For the second node:**

$$\dot{Q}_h - P_{TE,e1} - \dot{Q}_{TE,e2} - \dot{Q}_{filler,e2} - \dot{Q}_{Peltier,n2} + \frac{\dot{Q}_{Joule,e2}}{2} = 0 \quad (22)$$

$$P_{TE,e1} = V_{TE,e1}\, I \quad (23)$$

$$V_{TE,e1} = \frac{n\, S_{e1}\, (T_{n1} - T_{n2})}{2} \quad (24)$$

$$\dot{Q}_{TE,e2} = \frac{T_{n2} - T_{n3}}{R_{t,TE,e2}} \quad (25)$$

$$\dot{Q}_{filler,e2} = \frac{T_{n2} - T_{n3}}{R_{t,filler,e2}} \quad (26)$$

$$\dot{Q}_{Peltier,n2} = n\, S_{e2}\, T_{n2}\, I \quad (27)$$

$$\dot{Q}_{Joule,e2} = I^2\, R_{e,TE,e2} \quad (28)$$

**For the third node:**

$$\dot{Q}_h - P_{TE,e1} - P_{TE,e2} - \dot{Q}_{TE,e3} - \dot{Q}_{filler,e3} - \dot{Q}_{Peltier,n3} + \frac{\dot{Q}_{Joule,e3}}{2} = 0 \quad (29)$$

$$P_{TE,e2} = V_{TE,e2}\, I \quad (30)$$

$$V_{TE,e2} = \frac{n\, S_{e2}\, (T_{n2} - T_{n3})}{2} \quad (31)$$

$$\dot{Q}_{TE,e3} = \frac{T_{n3} - T_{n4}}{R_{t,TE,e3}} \quad (32)$$

$$\dot{Q}_{filler,e3} = \frac{T_{n3} - T_{n4}}{R_{t,filler,e3}} \quad (33)$$

$$\dot{Q}_{Peltier,n3} = n\, S_{e3}\, T_{n3}\, I \quad (34)$$

$$\dot{Q}_{Joule,e3} = I^2\, R_{e,TE,e3} \quad (35)$$

**For the forth node:**

$$\dot{Q}_h - P_{TE,e1} - P_{TE,e2} - P_{TE,e3} - \dot{Q}_{TE,e4} - \dot{Q}_{filler,e4} - \dot{Q}_{Peltier,n4} + \frac{\dot{Q}_{Joule,e4}}{2} = 0 \quad (36)$$

$$P_{TE,e3} = V_{TE,e3}\, I \quad (37)$$

$$V_{TE,e3} = \frac{n\, S_{e3}\, (T_{n3} - T_{n4})}{2} \quad (38)$$

$$\dot{Q}_{TE,e4} = \frac{T_{n4} - T_{n5}}{R_{t,TE,e4}} \quad (39)$$

$$\dot{Q}_{filler,e4} = \frac{T_{n4} - T_{n5}}{R_{t,filler,e4}} \quad (40)$$

$$\dot{Q}_{Peltier,n4} = n\, S_{e4}\, T_{n4}\, I \quad (41)$$

$$\dot{Q}_{Joule,e4} = I^2\, R_{e,TE,e4} \quad (42)$$

**For the fifth node:**

$$\dot{Q}_h - P_{TE,e1} - P_{TE,e2} - P_{TE,e3} - P_{TE,e4} - \dot{Q}_c = 0 \quad (43)$$

$$P_{TE,e4} = V_{TE,e4}\, I \quad (44)$$

$$V_{TE,e4} = \frac{n\, S_{e4}\, (T_{n4} - T_{n5})}{2} \quad (45)$$

$$\dot{Q}_c = \frac{T_{n5} - T_c}{R_{t,c}} \quad (46)$$

In Eq. 17, the average temperature of the absorber surface in each section is shown by $T_h$. Temperature of i$^{th}$ node is shown by $T_{ni}$, thus the temperatures at the hot and cold junctions are given by $T_{n1}$ and $T_{n5}$, respectively. In these equations, number of thermocouples is shown by $n$, the fill factor of active thermoelectric material is defined by $FF$, the connection area of each TEG unit to the absorber surface is shown by $A_{tot}$ and the net Seebeck coefficient in i$^{th}$ element ($S_{ei}$) is defined as $S_{p,ei}$-$S_{n,ei}$. The fill factor in a TE module is defined as the ratio of the total cross sectional area of the thermoelectric legs over the area of the ceramic plate. Herein, $S_{p,ei}$ and $S_{n,ei}$ are the Seebeck coefficient of the p-leg and n-leg, respectively. Due to square shape of the thermoelectric heat recovery unit in each section of the absorber, surface area of every section is constant. Parameters $V_{TE,ei}$ and $P_{TE,ei}$ express the thermoelectric voltage and electrical power generated by the i$^{th}$ element. The electrical current, electrical resistance of the i$^{th}$ element and the total electrical resistance of the TEG module is shown by $I$, $R_{e,TE,ei}$ and $R_{e,tot}$, respectively. The electrical current is calculated by dividing the total generated Seebeck voltage to summation of the TEG internal resistance and the applied electrical load. To achieve theoretical matched power output (peak power point- PPP), the external electrical load is taken equal to the internal resistance of the TEG (Mirhosseini et al. 2017a, 2017b, 2018a, 2019a). In this study, the electrical resistance is set to obtain the peak power point (PPP). The parallel thermal resistances of the filler and thermoelectric materials at i$^{th}$ element is depicted by $R_{t,filler,ei}$ and $R_{t,TE,ei}$. Therefore:

$$R_{e,TE,ei} = 2\, n\, \rho_{TE,ei} \left(\frac{l_{TE,ei}}{A_{leg}}\right) \quad (47)$$

$$R_{e,tot} = R_{e,TE,e1} + R_{e,TE,e2} + R_{e,TE,e3} + R_{e,TE,e4} + R_{e,tot,IC} + R_{e,tot,contact} \quad (48)$$

$$I = \frac{n\, S_{e1}(T_{n1} - T_{n2}) + n\, S_{e2}(T_{n2} - T_{n3}) + n\, S_{e3}(T_{n3} - T_{n4}) + n\, S_{e4}(T_{n4} - T_{n5})}{R_{e,tot} + R_{e,load}} \quad (49)$$

$$R_{t,TE,ei} = \frac{l_{TE,ei}}{k_{TE,ei}\, A_{tot}\, FF} \tag{50}$$

$$R_{t,filler,ei} = \frac{l_{TE},ei}{k_{filler}\, A_{tot}(1-FF)} \tag{51}$$

$$n = \frac{A_{tot}\, FF}{2\, A_{leg}} \tag{52}$$

$$R_{e,tot,IC} = 2\, n\, \rho_{IC}\, \frac{\sqrt{\frac{1}{FF}+1}}{t_{IC}} \tag{53}$$

$$R_{e,tot,contact} = 4\, n\, \frac{\rho_{contact}}{A_{leg}} \tag{54}$$

where $l_{TE,ei}$ is the thermoelectric leg length and $k_{TE,ei}$ is thermal conductivity of the thermoelectric material in i$^{th}$ element. In the model, thermal conductivity of the filler ($k_{filler}$), total electrical resistance of interconnection ($R_{e,tot,IC}$) and electrical contact resistance ($R_{e,tot,contact}$) are applied. The electrical resistivity of thermoelectric material, interconnections, and contacts are represented by $\rho_{TE}$, $\rho_{IC}$, and $\rho_{contact}$, respectively. The area of each thermoelectric leg is expressed by $A_{leg}$. Parameter $l_c$ is the thicknesses of the ceramic layer for both hot and cold sides. The thermal conductivity of the ceramic layers is represented by $k_c$. As mentioned, expression of the $R_{t,c}$ has two parts, thermal resistances related to the heat conduction through the ceramic layer and the heat transferred to the ambient by convection. Therefore:

$$R_{t,h} = \frac{l_c}{k_c\, A_{tot}} \tag{55}$$

$$R_{t,c} = \frac{l_c}{k_c\, A_{tot}} + R_{t-heat\ sink} \tag{56}$$

The coupled system of Eqs. (16-56) is solved by number of iterations to find the temperatures in the nodes along the TEG legs. By assuming same external load and revealing the unknown temperatures at both hot and cold junctions, the matched power output can be obtained. This relation is applicable in the form of Eq. 57, when the radiative and convective heat losses from the thermoelectric elements to the neighbour elements and ambient are neglected. The energy conversion efficiency is calculated as a fraction of the total power generation over the heat input of the hot junction of the TEG.

$$P_{Matched} = \dot{Q}_h - \dot{Q}_c \tag{57}$$

$$\eta = \frac{P}{\dot{Q}_h} \tag{58}$$

The temperature dependent properties of the thermoelectric materials such as Seebeck coefficient ($\alpha$), thermal conductivity ($k$) and electrical resistivity ($\rho$) for both $Zn_4Sb_3$ and $Mg_2SiSn$ are given by polynomial equations. The coefficients are shown in Table 5. The nominal parameters utilized to build the model are given in Table 6.

Table 5: Thermo-electrical properties of p- and n-type materials fitted by polynomial equations ($a_3T^3+a_2T^2+a_1T+a_0$) (Rezania et al., 2014)

| Constant | $a_3$ | $a_2$ | $a_1$ | $a_0$ |
|---|---|---|---|---|
| **$Zn_4Sb_3$** | | | | |
| α (V/K) | 0 | $-6\times10^{-10}$ | $8.08\times10^{-7}$ | $-9.52\times10^{-5}$ |
| k (W/mK) | 0 | 0 | $-1.3\times10^{-4}$ | $8.6\times10^{-1}$ |
| ρ (Ωm) | $-5\times10^{-13}$ | $5\times10^{-10}$ | $-1.47\times10^{-7}$ | $2.465\times10^{-5}$ |
| **$Mg_2SiSn$** | | | | |
| α (V/K) | | | $-2.644\times10^{-7}$ | $-7.5249\times10^{-6}$ |
| k (W/mK) | | | $-2.6\times10^{-3}$ | 3.64 |
| ρ (Ωm) | | $2\times10^{-11}$ | $3\times10^{-9}$ | $4.624\times10^{-6}$ |

Table 6: Assumed parameters for mathematical modelling

| | |
|---|---|
| Diameter of the kiln | 3.6 m |
| Outer diameter of the absorber ($D_0$) | 5.05 m |
| Total absorber length | 6.542 m |
| Absorber length for each section | 0.6542 m |
| Absorber thickness | 2.5 cm |
| Absorber width | 0.6542 m |
| Ceramic layer thickness ($l_c$) | 0.5 mm |
| Thermal conductivity of ceramic layer | 30 W/mK |
| Thermal conductivity of filler, air ($k_{filler}$) | 0.024 W/mK |
| Individual leg cross sectional area ($A_{leg}$) | $4\times10^{-6}$ $m^2$ |
| Semiconductor/metal electrical contact resistivity ($\rho_{contact}$) | $5\times10^{-11}$ $\Omega m^2$ |
| Au interconnect thickness ($t_{IC}$) | 100 μm |
| Electrical resistivity of interconnections ($\rho_{IC}$) | $2.44\times10^{-8}$ Ωm |

## 5. Economic evaluation

Following calculation of the maximum power generation from the ten thermoelectric units, an economic evaluation for them is furthermore carried out to find the financial feasibility of the system. Different types of costs in economic evaluation of a thermoelectric system have been considered previously (Benday et al. 2017; Kishita et al. 2016; LeBlanc 2014; LeBlanc et al. 2014; Yee et al. 2013). In this study, various cost contributions

have been extracted from the literature and are combined in order to more accurate estimation of the cost.

There is collection of costs for a TEG system including bulk raw material cost ($C_B$), manufacturing cost associated with processing bulk material ($C_{M,B}$), areal manufacturing cost ($C_{M,A}$), heat exchanger cost ($C_{H\text{-}EX}$), balance of system cost ($C_{BoS}$) and installation cost ($C_I$). To fabricate a bulk module in this study using $Zn_4Sb_3$ and $Mg_2SiSn$, spark plasma sintering (SPS) is considered as bulk material manufacturing process, and dicing (D), metallization (M), medium level microfabrication (MLM) and screen printing (SP) are consisted in areal manufacturing processes. One of the main advantages of the solid state TEG systems is that, after installation there is no need for maintenance, hence the operation and maintenance cost can usually be ignored. The total cost of the TEG system is formulated as follows:

$$C_{tot} = C_B + C_{M,B} + C_{M,A} + C_{H-EX} + C_{BoS} + C_I \quad (59)$$

$$C_B = C_B^* \rho LAF \quad (60)$$

$$C_{M,B} = C_{M,B}^* \rho LAF = C_{SPS}^* \rho LAF \quad (61)$$

$$C_{M,A} = C_{M,A}^* AF = (C_D^* + C_M^* + C_{MLM}^* + C_{SP}^*) AF \quad (62)$$

$$C_{H-EX} = C_{H-EX}^* \left(\frac{1}{R_{H-EX}}\right) \quad (63)$$

$$C_{BoS} = 0.1 \left(C_B + C_{M,B} + C_{M,A} + C_{H-EX}\right) \quad (64)$$

$$C_I = 0.1 \left(C_B + C_{M,B} + C_{M,A} + C_{H-EX}\right) \quad (65)$$

where $C_B^*$ is average price per unit mass of the bulk thermoelectric materials, 4 (\$/kg)); $C_{M,B}^*$ is the bulk material processing cost per unit mass of the thermoelectric materials that is equal to $C_{SPS}^*$, 1.3 (\$/kg). The parameter $C_{M,A}^*$ is the areal manufacturing cost per unit area of the TEG module. The specific areal cost consists of dicing cost per unit area ($C_D^*$), 47 (\$/m$^2$); metallization cost per unit area ($C_M^*$), 120 (\$/m$^2$); medium level of microfabrication per unit area ($C_{MLM}^*$), 2500 (\$/m$^2$); and screen printing cost per unit area ($C_{SP}^*$), 4.8 (\$/m$^2$). The parameter $C_{H-EX}^*$ represents combined ceramic plates (at the hot and cold sides of the TEG module) and specific costs of the heat exchangers. In order to calculate the cost of this part, $C_{H-EX}^*$ (18.48 \$/(W/K)) is multiplied to the reverse of the total thermal resistance of the ceramic plates and the heat exchanger, $R_{H-EX}$ (K/W).

The balance of the system and installation costs are estimated 10% of the total cost of the TEG system in each section. Where $\rho$, $L$, $A$, and $F$ are thermoelectric materials' average density (kg/m$^3$), optimum leg length corresponding to the maximum peak power point, area of one side of the TEG module, and fill factor.

## 6. Experimental validation

The first part of the current study is to simulate the heat transfer around the rotary cement kiln and the arc absorber to find the temperature distribution along the absorber circumference. In section 2 of this paper, an

analytical solution for the real kiln without absorber was done showing a good agreement with the numerical solution. Moreover, precision of the adapted numerical procedure is shown in previous works (Mirhosseini et al. 2018b; Mirhosseini et al. 2019b).

The second part is to model and optimize the TEG units by using one dimensional finite element method (1D-FEM) in steady state condition. In order to validate the modelling procedure, a commercially available $Bi_2Te_3$ thermoelectric module mounted between a hot side block and a cold forged pin-fin heat sink consisting of 9×9 fins was tested. The properties of thermoelectric materials are given by the module manufacturer. Various temperatures can be provided by a heater in the hot side block. An axial fan is used for force convection cooling of the heat sink. A DC power supply is utilized to make different air flow rates in the heat sink. The free stream air velocity is measured by a hot wire anemometer (Swema 3000) at front of the heat sink. The device has also capability of measuring the air stream temperature. A K-type thermocouple is placed behind the hot side of the TE module to measure the temperature. A 127 μm thick graphite sheet is used between the hot side of the thermoelectric module and the hot block and also between the cold side of the module and base plate of the heat sink to reduce thermal contact resistance. The temperature, output voltage and current of the TEG are the main parameters which are collected by a Keysight 34972A LXI Data Acquisition system. A programmable DC electronic load device (B&K PRECISION, model 8500, 300 W) is used for applying different electrical loads on the thermoelectric module. Fig. 4 shows the test rig and the test components. Different parameters such as boundary conditions and size of the components used in the validation are shown in Table 7.

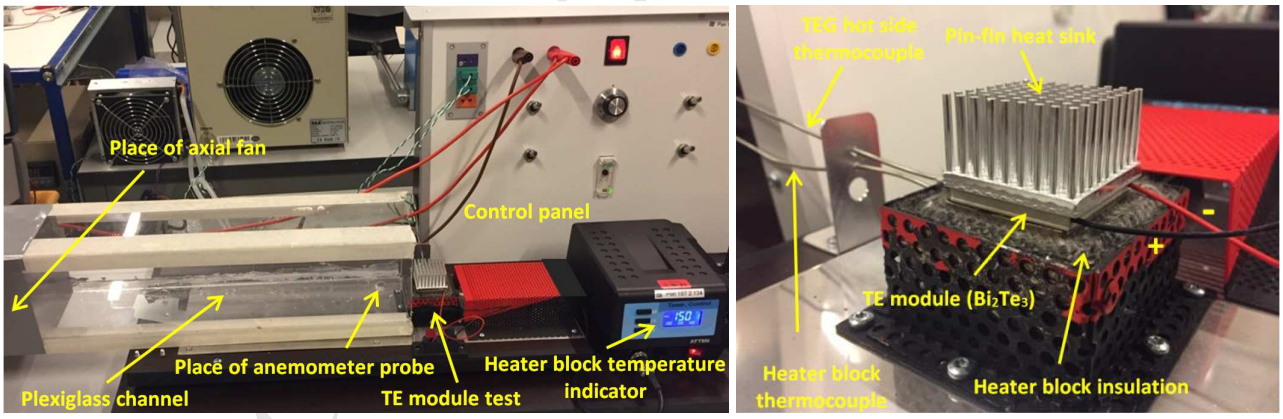


(a) (b)

Fig. 4: (a) A picture of the experimental setup for the validation, (b) Thermoelctric module test section and its components

Table 7: Dimensions of the device and conditions used in the experiments

| | | | |
|---|---|---|---|
| TE module size | 3 cm × 3 cm | Hot side temperature of TE module | 120, 170, 220 °C |
| Leg length | 1.5 mm | Pin diameter | 1.8 mm |
| Leg cross sectional size | 1 mm × 1 mm | Fin height | 16.5 mm |
| Thermoelectric couple number | 127 | Base thickness | 3.5 mm |
| Fill factor | 28.2 % | Heat sink length | 3.27 cm |
| Au interconnect thickness ($t_{IC}$) | 5 μm | Heat sink width | 3.27 cm |
| Free stream air temperature | 23 °C | $S_L$ | 3.634 mm |
| Free stream air velocity | 1, 1.5, 2 m/s | $S_W$ | 3.634 mm |

By considering geometrical properties of the thermoelectric module, heat sink and boundary conditions in the theoretical model (as formulated in section 4 of this paper), a good agreement has been seen between the experimental and modelling results. This agreement is shown in Fig. 5 by comparing the values of the matched power output for various hot side temperatures of the thermoelectric module and the free stream air velocity.

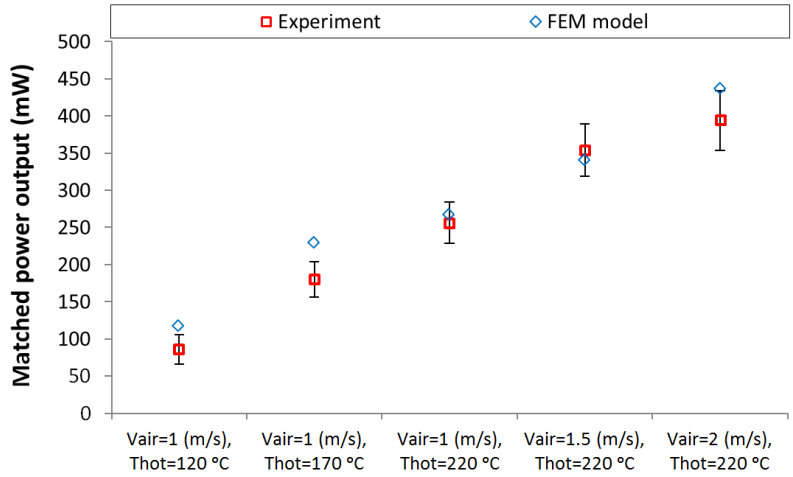


Fig. 5: Matched power output for different operating conditions; experimental data (including standard deviation) and theoretical model results.

## 7. Results and discussions

The TEGs in the heat recovery system are optimized based on the leg length and fill factor. The results show that

for each fill factor there is an individual leg length providing maximum power generation in the TEG. By selecting the heat sink I, the results of the matched power output obtained for the first section are shown in Fig. 6. As can be seen, the maximum matched power output increases from FF=0.01 to FF=0.9. At the small leg lengths, the maximum power increases rapidly with variation of the leg length, however this increment is slighter for high fill factors. Comparison of the maximum matched power outputs shows that, the results of fill factor higher than 0.2 may not be economically a good choice among the studied cases. In fill factor of 0.5, for example, the optimum leg length is higher than 2 times compared to that one for FF=0.2, while the maximum matched power increases only to some extent. Therefore, three fill factors, namely 0.05, 0.1, and 0.2, are selected for further detailed consideration in this study. For the other sections and using two other heat sinks, the results represent the similar trend.

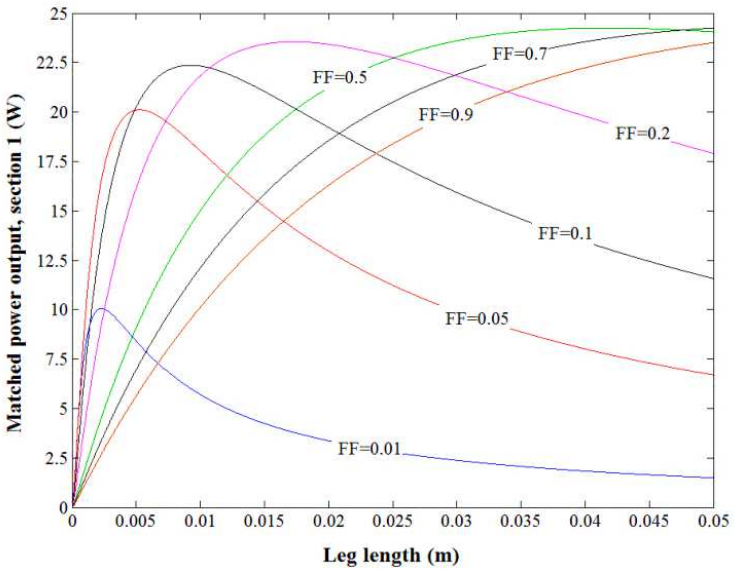


Fig. 6: Matched power output for the first thermoelectric unit by using heat sink I

*7.1. Power optimization for different pin-fin heat sinks*

From Fig. 6 and the results related to nine other units which have not been shown here, the design parameters corresponding to the maximum matched power output are selected for three effective fill factors. The temperature difference between the hot and cold junctions of the thermoelectric leg decreases as fill factor increases. By increasing the fill factor, the thermal resistance of the TEG reduces, therefore the heat flux across

the leg enhances. Although the design of heat sink for each section is fixed, the two junctions' temperature difference of the TEGs is different to each other. The reason is for different boundary conditions due to velocity and temperature distribution of the air corresponding to the heat sink position. As Fig. 1 shows, the highest temperature on the absorber occurs in 9$^{th}$ section, while the highest temperature difference across the TEGs (Fig. 7a) is observed in 7$^{th}$ section, due to condition of the air flow in heat sinks, which significantly affects performance of the TEG units. In Fig. 7b, the optimum leg length corresponding to the maximum peak power point is shown. This parameter increases in higher fill factors, particularly in the first and last sections. The results in Fig. 7c represent that the TEG units can generate electrical power from 20 W to 50 W in the considered sections. The total power is summation of local power captured by TEG units that is 323.42, 366.51, and 389.57 W for fill factor of 0.05, 0.1, and 0.2, respectively. Change of power from FF=0.1 to 0.2 is less than it from FF=0.05 to 0.1. Figure 7d indicates the energy conversion efficiency in different units along the absorber circumference. Although, the power distribution is approximately symmetric among all studied fill factors, the efficiency distribution shows the highest magnitudes where the heat source temperature (see Fig. 1) is highest (9$^{th}$ section). The average efficiency is almost 1.21 %, 1.29 %, and 1.33 % for FF=0.05, 0.1, and 0.2, respectively. The number of the thermoelectric couples in each TEG unit is 2674, 5349 and 10699 for fill factors of 0.05, 0.1 and 0.2, respectively.

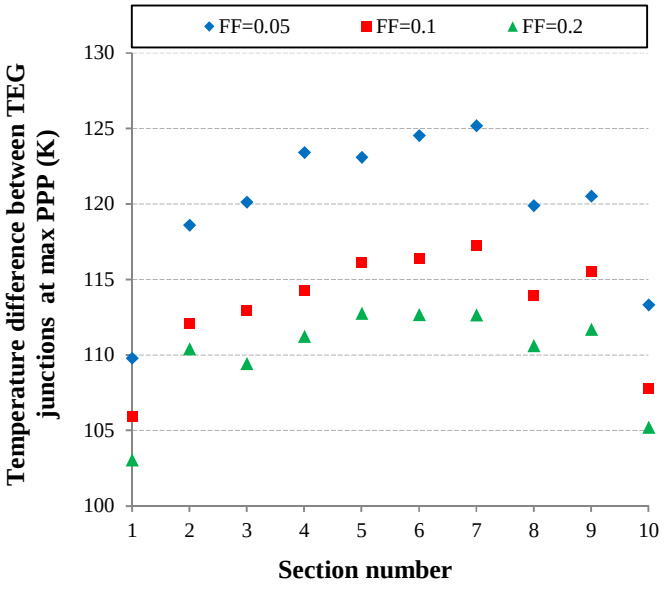


(a)

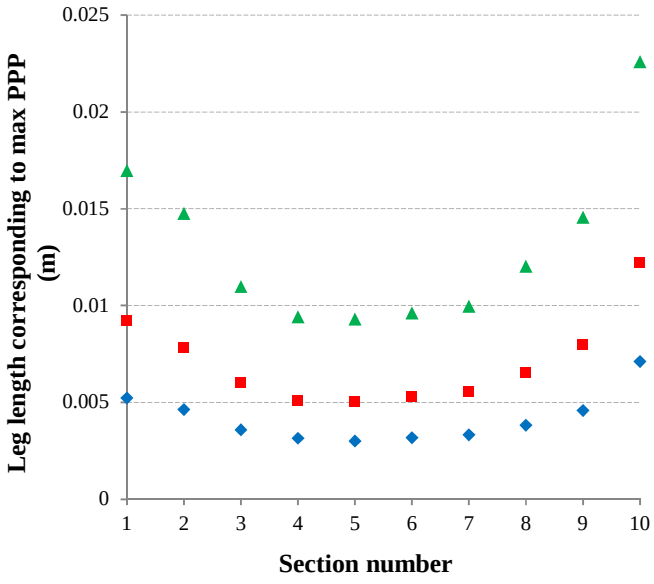


(b)

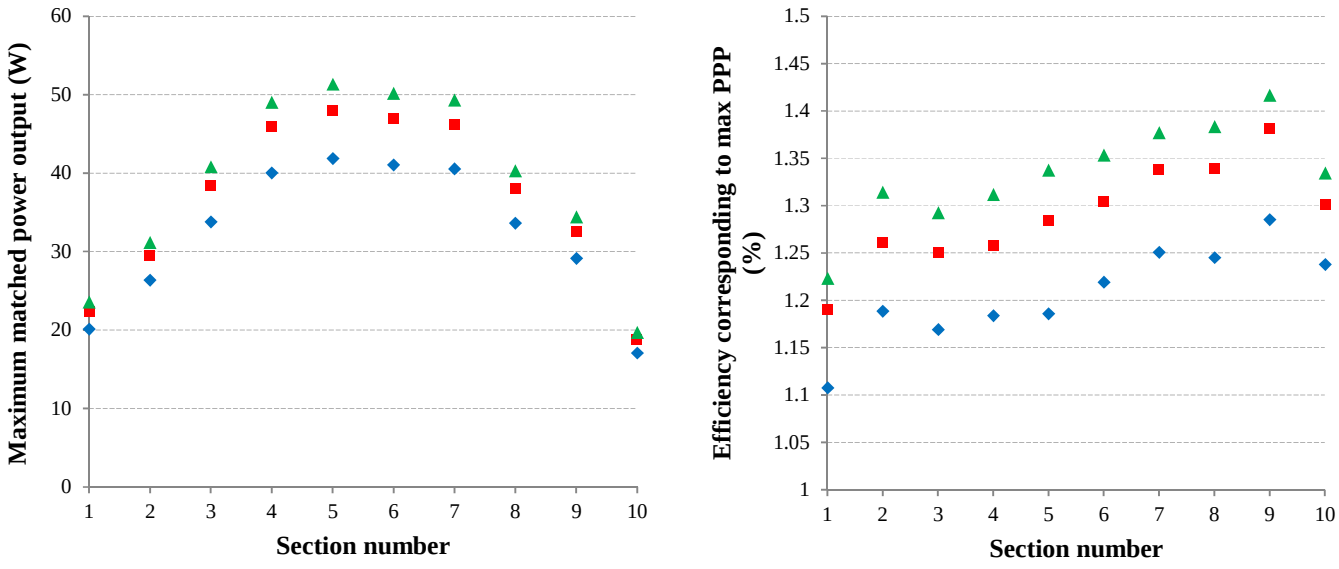


(c) (d)

Fig. 7: Performance of TEG system by using the heat sink I, (a) temperature difference, (b) leg length, (c) maximum matched power, (d) efficiency

With the same procedure, Tables 8 and 9 show the results of utilizing two other heat sinks (II and III). In Table 8, the height of the pin-fin is set to 10 mm and both of the $S_L$ and $S_W$ are assumed equal to 65.42 mm. The shorter pin-fin with larger distance between the fins causes an increase in the thermal resistance of the heat sink. Therefore, the temperature difference between two junctions reduces as shown in Table 8. In addition, the peak power output distributions reduces significantly, however the average efficiency value of the TEG system slightly increases, because of reduction of the heat flux across the modules. In this case, the average efficiency is approximately 1.22 %, 1.30 %, and 1.35 % for FF=0.05, 0.1 and 0.2, respectively. Moreover, the total power of the system at maximum matched power is 136.544, 149.606, and 156.497 W, respectively, corresponding to the mentioned fill factors. The difference percentage between these values compared with the results by the heat sinks I and II is 57.8 %, 59.18 %, and 59.83 %, respectively for fill factors of 0.05, 0.1 and 0.2.

Table 8: Performance of TEG system at maximum PPP by using the heat sink II: temperature difference between TEG junctions, leg length, maximum matched power output, efficiency

| | FF | Section number | | | | | | | | | |
|---|---|---|---|---|---|---|---|---|---|---|---|
| | | 1 | 2 | 3 | 4 | 5 | 6 | 7 | 8 | 9 | 10 |
| ΔT (K) | 0.05 | 103.38 | 111.82 | 115.8 | 116.42 | 117.49 | 120.2 | 120.28 | 111.95 | 114.07 | 107.47 |

| | | | | | | | | | | | |
|---|---|---|---|---|---|---|---|---|---|---|---|
| | 0.1 | 104.3 | 110.14 | 110.84 | 112.48 | 112.94 | 113.57 | 115 | 111.35 | 113.26 | 107.22 |
| | 0.2 | 102.37 | 109.69 | 109.74 | 110.67 | 111.24 | 112.37 | 113.5 | 110.16 | 112.76 | 106.63 |
| LL (mm) | 0.05 | 13.78 | 11.56 | 8.36 | 6.52 | 6.32 | 7.00 | 7.44 | 8.74 | 11.72 | 20.94 |
| | 0.1 | 26.4 | 21.18 | 14.5 | 11.52 | 11.06 | 11.84 | 12.88 | 16.32 | 21.8 | 39.26 |
| | 0.2 | 49.42 | 40.74 | 27.6 | 21.68 | 20.86 | 22.52 | 24.38 | 31.02 | 41.92 | 75.3 |
| Max PPP (W) | 0.05 | 7.17 | 9.98 | 14.44 | 18.53 | 19.56 | 18.74 | 18.00 | 13.77 | 10.89 | 5.47 |
| | 0.1 | 7.76 | 10.83 | 15.82 | 20.44 | 21.6 | 20.65 | 19.79 | 15.03 | 11.81 | 5.88 |
| | 0.2 | 8.07 | 11.28 | 16.55 | 21.44 | 22.67 | 21.66 | 20.73 | 15.7 | 12.3 | 6.10 |
| η (%) | 0.05 | 1.1 | 1.19 | 1.2 | 1.2 | 1.22 | 1.26 | 1.29 | 1.24 | 1.29 | 1.23 |
| | 0.1 | 1.2 | 1.27 | 1.27 | 1.28 | 1.3 | 1.32 | 1.36 | 1.35 | 1.39 | 1.32 |
| | 0.2 | 1.23 | 1.32 | 1.31 | 1.32 | 1.34 | 1.37 | 1.4 | 1.4 | 1.44 | 1.36 |

As expected, by using staggered configuration instead of in-line arrangement, the air flow around the fins becomes more turbulent and hence the thermal resistance of the heat sink reduces. The temperature difference between two junctions and the total power increase. For the staggered case (in Table 9), the generated power by the system is entirely 371.38, 424.51, and 453.28 W for FF=0.05, 0.1 and 0.2, which show the growth of 14.8 %, 15.82 % and 16.35 % than the results of heat sink I, respectively.

Also, energy conversion efficiency of 1.20 %, 1.29 % and 1.34 % is obtained so that is approximately equal to the results of the first and second pin-fin heat sinks. A comparison between these three cases of heat exchangers illustrates that whatever the thermal resistance of the heat sink is lower; the maximum matched power output is higher. The heat sink thermal resistance has significant effect on power generation; however it does not affect the efficiency comparatively.

Table 9: Performance of TEG system at maximum PPP by using the heat sink III: temperature difference between TEG junctions, leg length, maximum matched power output, efficiency

| | FF | Section number | | | | | | | | | |
|---|---|---|---|---|---|---|---|---|---|---|---|
| | | 1 | 2 | 3 | 4 | 5 | 6 | 7 | 8 | 9 | 10 |
| Δ T (K) | 0.05 | 112.65 | 119.37 | 119.81 | 124.44 | 125.09 | 125.68 | 127.06 | 120.81 | 123.57 | 113.3 |
| | 0.1 | 106.91 | 112.43 | 114.03 | 115.84 | 118.19 | 118.7 | 118.63 | 114.55 | 116.7 | 108.92 |
| | 0.2 | 104.49 | 110.73 | 111.12 | 111.9 | 113.62 | 114.1 | 114.34 | 111.08 | 113.37 | 107.2 |
| LL (mm) | 0.05 | 4.74 | 4.02 | 3.04 | 2.72 | 2.64 | 2.76 | 2.92 | 3.32 | 4.14 | 6.18 |
| | 0.1 | 8.08 | 6.76 | 5.22 | 4.46 | 4.46 | 4.66 | 4.82 | 5.66 | 7.00 | 10.82 |

| | | | | | | | | | | | |
|---|---|---|---|---|---|---|---|---|---|---|---|
| | 0.2 | 15.02 | 12.76 | 9.66 | 8.12 | 8.04 | 8.4 | 8.74 | 10.38 | 12.88 | 20.38 |
| Max PPP (W) | 0.05 | 23.04 | 30.23 | 38.83 | 46.02 | 48.07 | 47.19 | 46.58 | 38.58 | 33.4 | 19.44 |
| | 0.1 | 25.78 | 34.07 | 44.47 | 53.27 | 55.73 | 54.53 | 53.63 | 43.95 | 37.61 | 21.47 |
| | 0.2 | 27.23 | 36.13 | 47.52 | 57.24 | 59.94 | 58.54 | 57.46 | 46.83 | 39.85 | 22.54 |
| η (%) | 0.05 | 1.12 | 1.18 | 1.15 | 1.17 | 1.18 | 1.21 | 1.25 | 1.24 | 1.3 | 1.23 |
| | 0.1 | 1.19 | 1.26 | 1.25 | 1.26 | 1.29 | 1.32 | 1.34 | 1.34 | 1.39 | 1.31 |
| | 0.2 | 1.24 | 1.31 | 1.31 | 1.31 | 1.34 | 1.36 | 1.39 | 1.38 | 1.43 | 1.35 |

*7.2. Optimization based on cost per power output*

The total cost of thermoelectric system is shown in Table 10 for three types of the heat sinks. With all the heat sinks, as the fill factor increases, the optimal leg length corresponding to the maximum peak power increases, which causes higher total cost. The heat exchanger cost does not change versus fill factor. However, in the second case, namely using the heat sink II, the total cost reduces significantly. The cooling capability of the heat sink in this case reduces due to the higher thermal resistance. According to Eq. 63, the heat sink cost decreases. Comparing results of heat sink I and II shows that, the dominant factor in the system cost is the heat sink. Therefore, a careful design strategy in order to minimize the heat sink cost is necessary in such a heat recovery system. For the heat sink III, which possesses the same geometrical parameters as the first heat sink except a staggered arrangement instead of the in-line, the total cost is approximately close to the first heat sink, although the cost of the staggered configuration is higher. It is worthy to note that, due to lower value of thermal resistance in staggered heat sink in comparison with the in-line, and referring to Eq. 63, the staggered configuration of pin-fins is more costly.

Table 10: Total cost ($) of TEG system corresponding to maximum matched power output for different applied heat sinks

| | FF | Section number | | | | | | | | | |
|---|---|---|---|---|---|---|---|---|---|---|---|
| | | 1 | 2 | 3 | 4 | 5 | 6 | 7 | 8 | 9 | 10 |
| Heat sink I | 0.05 | 419.86 | 476.58 | 606.98 | 704.74 | 719.49 | 688.87 | 654.78 | 563.15 | 465.07 | 326.07 |
| | 0.1 | 497.43 | 552.68 | 681.31 | 778.15 | 792.93 | 762.46 | 728.64 | 638.05 | 541.41 | 406.41 |
| | 0.2 | 668.25 | 719.40 | 840.22 | 934.04 | 948.56 | 918.68 | 885.43 | 799.06 | 707.37 | 588.52 |
| Heat sink II | 0.05 | 195.95 | 221.62 | 289.22 | 346.22 | 355.12 | 336.18 | 315.56 | 263.96 | 215.89 | 160.66 |
| | 0.1 | 291.08 | 311.16 | 371.86 | 426.05 | 434.47 | 416.13 | 396.62 | 348.82 | 306.17 | 268.41 |
| | 0.2 | 526.79 | 530.36 | 564.41 | 606.56 | 613.37 | 598.48 | 582.61 | 548.19 | 527.74 | 557.01 |

| | | | | | | | | | | | |
|---|---|---|---|---|---|---|---|---|---|---|---|
| Heat sink III | 0.05 | 474.46 | 542.39 | 697.51 | 812.68 | 830.43 | 793.35 | 753.4 | 644.22 | 528.87 | 362.77 |
| | 0.1 | 550.83 | 617.45 | 771.14 | 885.5 | 903.31 | 866.42 | 826.57 | 718.26 | 604.18 | 441.89 |
| | 0.2 | 717.9 | 780.17 | 927.53 | 1038.73 | 1056.32 | 1020.14 | 981 | 876 | 766.9 | 619.81 |

The maximum peak power output increases with the fill factor. Therefore, a higher fill factor is an advantage in the heat recovery system. Furthermore, the total cost has an incremental trend by increasing the fill factor. Therefore, it leads to a more expensive TEG system. Nevertheless, the question is that what fill factor is the most efficient value from both aspects of the power generation and cost. A trade-off between the matched power output and the total cost can identify the optimum fill factor for both of the power and the cost. Therefore, cost per power is defined as the most appropriate criterion. In Fig. 8, this ratio is shown for the three fill factors and three types of heat sinks.

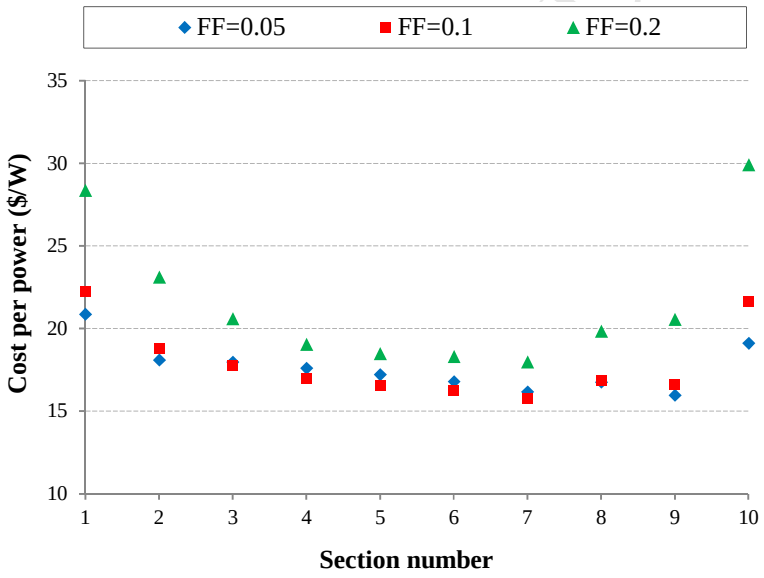


(a)

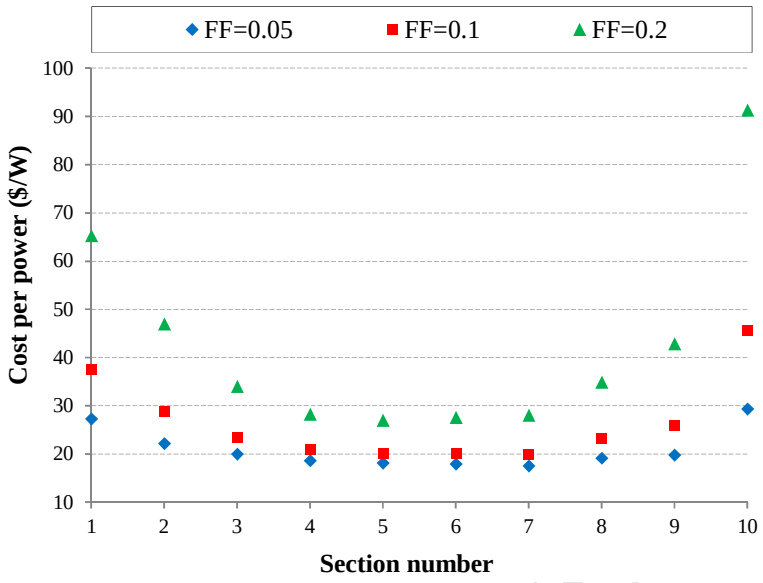


(b)

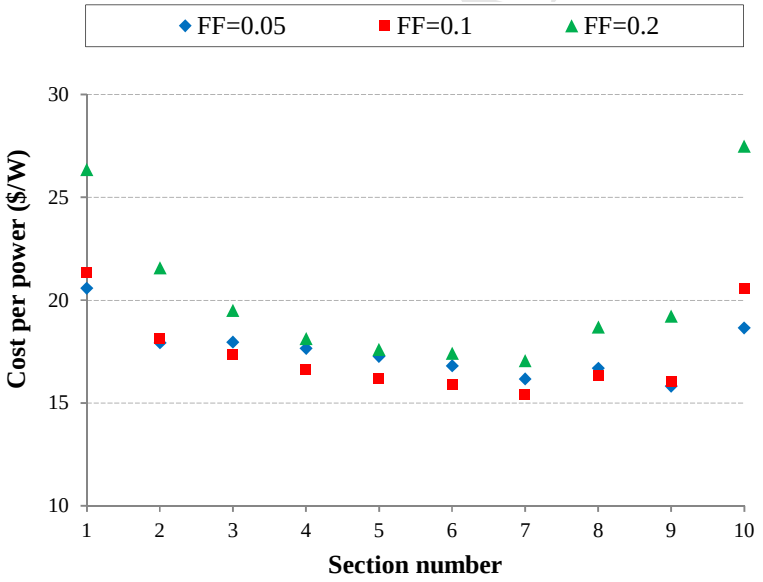


(c)

Fig. 8: Total cost per matched power output, (a) heat sink I, (b) heat sink II, (c) heat sink III.

The results shows that the fill factor of 0.2 can generate the highest power in comparison with 0.05 and 0.1, although, it causes the highest cost. In Fig. 8b, there is an incremental trend for the ratio of the cost to the power versus the fill factor. However, in Figs. 8a, and 8c, there is no individual fill factor applicable for all the sections

to minimize the cost per power. Evaluation of the data in Fig. 8a reveals that, for sections 3-7, fill factor of 0.1 and for the rest sections fill factor of 0.05 can be selected to have the highest techno-economical performance. Figure 8c shows that, the minimum cost per power occurs at fill factor of 0.1 in sections 3-8, since for the rest sections fill factor of 0.05 is chosen. It is worthy to mention that, among the considered heat sinks, the staggered configuration of the heat sinks (heat sink III) provides the lowest cost per power in the all sections along the absorber.

## 8. Conclusions

The lack of primary energy resources, growing global demand for consuming energy and increasing concern of environmental issues of emissions and pollutions accelerate the researches to find alternative green technologies for generating electrical power with cleaner processes. A large amount of industrial heat loss is related to the power utilities and manufacturing factories. Hence, optimization of the heat recovery system in this study was oriented towards harvesting energy from industrial waste heat such as cement factory. In this study, design of a waste heat recovery system from the cement kiln was performed by thermoelectric modules. A 5-node FEM model was developed to design and analyze the thermoelectric systems. To confirm the correctness of the model, an experimental setup in laboratory scale was built. The results showed that there is a good agreement between the experimental and modelling results. Then, the model was confidently used for this large scale engineering application of thermoelectric systems. Over a wide range of fill factor, the optimum leg length corresponding to the maximum peak power output was explored. Three types of pin-fin heat sinks were utilized to assess the cooling effect on the power optimization. The heat sink with staggered arrangement of pin-fins (heat sink III) represented the highest maximum matched power output, so that the average power generated by the whole TEG system was 86.78, 99.19, and 105.91 $W/m^2$ for fill factor of 0.05, 0.1 and 0.2, respectively.

The results showed that the main portion of the system cost is related to the heat exchanger. The total cost per power by using the heat sink III is the lowest in comparison with other heat sinks considered in this study. In this case, the average cost per power for the ten sections of the TEG system along the absorber circumference was obtained 17.56, 17.40, and 20.32 $/W, respectively for fill factors of 0.05, 0.1 and 0.2. The results of the present study are comparable with the new results and those reviewed in the previous paper of the authors (Mirhosseini et al. 2019b); however there are different approaches in their design parameters and assumptions such as material type, thermal absorber shape, mathematical modelling, and boundary conditions, etc. Furthermore, effect of different absorber shapes, thermoelectric materials, and heat sinks can be investigated in the future.

**Acknowledgment**

This work was carried out within the framework of the Center for Thermoelectric Energy Conversion (CTEC) and was funded in part by the Danish Council for Strategic Research, Programme Commission on Energy and

Environment, under Grant No. 1305-00002B. The authors acknowledge Aalborg Portland cement factory for providing the temperature distribution along the cement rotary kiln and primary information related to this study.

**References**

Benday, N.S., Dryden, D.M., Kornbluth, K., Stroevea, P., 2017. A temperature-variant method for performance modeling and economic analysis of thermoelectric generators: Linking material properties to real-world conditions. Appl. Energy. 190, 764-771. https://doi.org/10.1016/j.apenergy.2016.12.157.

Dunham, M.T., Barako, M.T., LeBlanc, S., Asheghi, M., Chen, B., Goodson, K.E., 2015. Power density optimization for micro thermoelectric generators. Energy. 93, 2006-2017. https://doi.org/10.1016/j.energy.2015.10.032.

Fernández-Yañez, P., Armas, O., Capetillo, A., Martínez-Martínez, S., 2018a. Thermal analysis of a thermoelectric generator for light-duty diesel engines. Appl. Energy, 226, 690-702. https://doi.org/10.1016/j.apenergy.2018.05.114.

Fernández-Yáñez, P., Armas, O., Kiwan, R., Stefanopoulou, A.G., Boehman, A.L., 2018b. A thermoelectric generator in exhaust systems of spark-ignition and compression-ignition engines. A comparison with an electric turbo-generator. Appl. Energy. 229, 80-87. https://doi.org/10.1016/j.apenergy.2018.07.107.

Fernández-Yáñez, P., Gómez, A., García-Contreras, R., Armas, O., 2018c. Evaluating thermoelectric modules in diesel exhaust systems: potential under urban and extra-urban driving conditions. J. Cleaner Prod. 182, 1070-1079. https://doi.org/10.1016/j.jclepro.2018.02.006.

Goudarzi, A., Mozaffari, A., Samadian, P., Rezania, A., Rosendahl, L.A., 2014. Intelligent design of waste heat recovery systems using thermoelectric generators and optimization tools. Meccanica. 49, 1211-1223. https://doi.org/10.1007/s11012-014-9878-0.

Hsiao, Y.Y., Chang, W.C., Chen, S.L., 2010. A mathematic model of thermoelectric module with applications on waste heat recovery from automobile engine. Energy. 35, 1447-1454. https://doi.org/10.1016/j.energy.2009.11.030.

Hsu, C.T., Won, C.C., Chu, H.S., Hwang, J.D., 2013. A case study of thermoelectric generator application on rotary cement furnace. 8th International Conference on Microsystems, Packaging, Assembly and Circuits Technology (IMPACT), 22-25 Oct. 2013, Taipei, Taiwan, IEEE Xplore. doi: 10.1109/IMPACT.2013.6706644.

Incropera, F.P., Dewitt, D.P., Bergman, T.L., Lavine, A.S., 2007. Fundamentals of Heat and Mass Transfer, Sixth ed.; John Wiley & Sons, USA, 2007; ISBN-13: 9780471457282.

Karellas, S., Leontaritis, A.D., Panousis, G., Bellos, E., Kakaras, E., 2013. Energetic and exergetic analysis of waste heat recovery systems in the cement industry. Energy. 58, 147-156. https://doi.org/10.1016/j.energy.2013.03.097.

Kishita, Y., Ohishi, Y., Uwasu, M., Kuroda, M., Takeda, H., Hara, K., 2016. Evaluating the life cycle $CO_2$ emissions and costs of thermoelectric generators for passenger automobiles: a scenario analysis. J. Cleaner Prod. 126, 607-619. https://doi.org/10.1016/j.jclepro.2016.02.121.

LeBlanc, S., 2014. Thermoelectric generators: Linking material properties and systems engineering for waste heat recovery applications. Sustainable Mater. Technol. 1–2, 26–35. https://doi.org/10.1016/j.susmat.2014.11.002.

LeBlanc, S., Yee, S.K., Scullin, M.L., Dames, C., Goodson, K.E., 2014. Material and manufacturing cost considerations for thermoelectrics. Renewable Sustainable Energy Rev. 32, 313–327. https://doi.org/10.1016/j.rser.2013.12.030.

Liu, J., Zhang, S., Wagner, F., 2018. Exploring the driving forces of energy consumption and environmental pollution in China's cement industry at the provincial level. J. Cleaner Prod. 184, 274-285. https://doi.org/10.1016/j.jclepro.2018.02.277.

Luo, Q., Li, P., Cai, L., Zhou, P., Tang, D., Zhai, P., Zhang, Q., 2015. A Thermoelectric waste-heat-recovery system for portland cement rotary kilns. J. Electron. Mater. 44, 1750-1762. https://doi.org/10.1007/s11664-014-3543-1.

Mirhosseini, M., Rezania, A., Blichfeld, A.B., Iversen, B.B., Rosendahl, L.A., 2017a. Experimental investigation of zinc antimonide thin film thermoelectric element over wide range of operating conditions, Phys. Status Solidi A, 214, 1700301. https://doi.org/10.1002/pssa.201700301.

Mirhosseini, M., Rezania, A., Iversen, B., Rosendahl, L., 2018a. Energy harvesting from a thermoelectric zinc antimonide thin film under steady and unsteady operating conditions. Materials. 11, 2365, 1-21. https://doi.org/10.3390/ma11122365.

Mirhosseini, M., Rezania, A., Rosendahl, L., Iversen, B.B., 2017b. Effect of thermal cycling on zinc antimonide thin film thermoelectric characteristics. Energy Procedia. 142, 519–524. https://doi.org/10.1016/j.egypro.2017.12.081.

Mirhosseini, M., Rezania, A., Rosendahl, L., 2018b. Numerical study on heat transfer to an arc absorber designed for a waste heat recovery system around a cement kiln. Energies. 11, 671. https://doi.org/10.3390/en11030671.

Mirhosseini, M., Rezania, A., Rosendahl, L., 2019a. Effect of heat loss on performance of thin film thermoelectric; A mathematical model. Mater. Res. Express. https://doi.org/10.1088/2053-1591/aafba1.

Mirhosseini, M., Rezania, A., Rosendahl, L., 2019b. Harvesting waste heat from cement kiln shell by thermoelectric system, Energy, 168, 358-369. https://doi.org/10.1016/j.energy.2018.11.109.

Ndao, S., Peles, Y., Jensen, M.K., 2009. Multi-objective thermal design optimization and comparative analysis of electronics cooling technologies. Int. J. Heat Mass Transfer. 52, 4317–4326. https://doi.org/10.1016/j.ijheatmasstransfer.2009.03.069.

Rezania, A., Rosendahl, L.A., 2011. Evaluating thermoelectric power generation device performance using a rectangular microchannel heat sink. J. Electron. Mater. 40, 481-488. https://doi.org/10.1007/s11664-011-1622-0.

Rezania, A., Rosendahl, L.A., 2012a. New configurations of micro plate-fin heat sink to reduce coolant pumping power. J. Electron. Mater. 41, 1298-1304. https://doi.org/10.1007/s11664-011-1887-3.

Rezania, A., Rosendahl, L.A., 2012b. Thermal effect of ceramic substrate on heat distribution in thermoelectric generators. J. Electron. Mater. 41, 1343-1347. https://doi.org/10.1007/s11664-012-1939-3.

Rezania, A., Rosendahl, L.A., Yin, H., 2014. Parametric optimization of thermoelectric elements footprint for maximum power generation. J. Power Sources. 255:151-156. https://doi.org/10.1016/j.jpowsour.2014.01.002.

Sztekler, K., Wojciechowski, K., Komorowski, M., Tarnowska, M., 2017. The thermoelectric generators use for waste heat utilization from cement plant, E3S Web of Conferences 2017; 14:01031. https://doi.org/10.1051/e3sconf/20171401031.

Touloukian, Y.S., Powell, R.W., Ho, C.Y., Klemens, P.G., 1970. Thermal Conductivity: Metallic Elements and Alloys, Purdue Research Foundation, Thermophysical Properties of Matter, Volume1, USA, https://apps.dtic.mil/dtic/tr/fulltext/u2/a951935.pdf

Yee, S.K., LeBlanc, S., Goodson, K.E., Dames, C., 2013. $ per W metrics for thermoelectric power generation: beyond ZT. Energy Environ. Sci. 6, 2561-2571. doi: 10.1039/C3EE41504J.

# Research highlights

- The best place along the rotary cement kiln is found for waste heat recovery purpose.
- Design and optimization of arc shaped thermoelectric system around the kiln is done.
- Temperature distribution on absorber as hot side reservoir of TEG is obtained by CFD.
- A mathematical model by FEM is developed to design the arc shaped TEG system.
- Various design parameters of TEG and pin-fin heat sink are studied.